B4(XQ3)LYP-APPROACH

RESULTS AND DISCUSSION

4

4.1 Spin multiplicity and the â₀ parameter in B4LYP

DFT-methods, fail often to describe the ground state multiplicities of TMCs correctly. Working on that problem, Reiher, Salomon and Hess[21, 22] found, that the energy splitting between high- and low-spin states of TMCs depends linearly on the exact exchange parameter [a_0 in Eq.(1.1)][21, 22]. They showed that the reduction of the exact exchange part E_x^X in the B3LYP functional to 15%, improves the functional (termed as B3LYP*) in respect to the prediction of the ground state spin multiplicities of TMCs. These findings were considered by the procedure of determination of the â₀ parameter in our approach.

The parameter â₀ of the exact exchange term was varied in a manner similar to that used with the B3LYP* functional of Reiher et al.[21], to enable the B4LYP functional [eq. (3.6)], to predict the correct spin multiplicity of the electronic ground states of TMCs. For this purpose, all model compounds (Table A3 of appendix) were selected, for which the B3LYP functional produced wrong spin multiplicities, obtained from the free energies G_g^o in vacuum [see eq. (3.4)]. These are eleven compounds (**4**, **6**, **11-13**, **15-19**, **25**, see Table 3). Compounds **7** and **8** were not considered in this analysis, since they exhibit spin-crossover behavior in solution[106, 130], indicating that the exact spin state depends on subtle interactions with the solvent.

Since the spin multiplicity of a TMC is generally measured in the condensed phase, the free energy in dielectric medium [G_s^o, eq. (3.2)] is the relevant quantity, and must be considered. Under these conditions, the conventional B3LYP functional yielded the correct spin multiplicity also for compounds **15** and **17**, which were therefore ignored in the following. For the remaining nine compounds (involving ten different redox states)

both G_g° and G_s° for the high- and low-spin states were computed using the B4LYP functional for different parameters â$_0$ (0.15, 0.13, 0.12, 0.11) fixing the other parameters at the conventional values a$_0$ = 0.20, a$_x$ = 0.72 and a$_c$ = 0.81 (Table 3).

Table 3. Total spin of electronic ground states of ten different TMCs in solution or crystal [one (**16**) in different redox states]. Except for compound **10,** these compounds were selected, since computations with the B3LYP DFT functional yielded ground state energies with wrong spin multiplicity. Computations were based on free energies [G_s°, eq. (3)] including the electrostatic energies in solutions. In cases where the spin multiplicities based on the free energies in vacuum [G_g°, eq. (5)] and dielectric medium [G_s°, eq. (3)] differed from each other, the computed spin multiplicities in vacuum were given in parenthesis.

	TMC	â$_0$ = a$_0$		â$_0$ [a$_0$ = 0.20]				exp.
		B3LYP	B3LYP*	B4LYP, eq (7)				
		0.20	0.15	0.15	0.13	0.12	0.11	
4	[Fe(phen)$_3$]$^{2+}$	2	0	0	0	0	0	**0**[131]
6	[Fe(sar)]$^{2+}$	2	0 (2)	0 (2)	0	0	0	**0**[132]
10	[Fe(PypepO)$_2$]$^{1-}$	5/2	5/2	5/2	5/2	5/2	1/2 (5/2)	**5/2**[109]
11	[Fe(PypepS)$_2$]$^{1-}$	5/2	1/2	1/2	1/2	1/2	1/2	**1/2**[110]
12	[Fe(PyAS)$_2$]^{0}	2	0	0	0	0	0	**0**[133]
13	[Fe(bpteta)$_2$]$^{2+}$	2	2	2	0 (2)	0 (2)	0	**0**[101]
16	[Fe(Prpep)$_2$]$^{1+}$	5/2	1/2	1/2	1/2	1/2	1/2	**1/2**[105]
16	[Fe(Prpep)$_2$]^{0}	2	2	2	2	0 (2)	0	**0**[105]
18	[Fe(PaPy$_3$)(Cl)]$^{1+}$	5/2	5/2	1/2 (5/2)	1/2	1/2	1/2	**1/2**[113]
19	[Fe(PaPy$_3$)(N$_3$)]$^{1+}$	5/2	1/2 (5/2)	1/2 (5/2)	1/2	1/2	1/2	**1/2**[113]
25	[Mn(CN)$_6$]$^{4-}$	5/2	1/2 (5/2)	1/2 (5/2)	1/2 (5/2)	1/2 (5/2)	1/2 (5/2)	**1/2**[134]

Among all tested $â_0$ parameters only at $â_0 = 0.12$, B4LYP yields the correct spin multiplicity for all considered compounds in Table 3 (the related energy data are given in Tables A2-A8 of appendix). With $â_0 = 0.15$ the B4LYP functional yields the same spin multiplicity in vacuum as does B3LYP* (Table 3). A further reduction of the $â_0$ parameter to 0.11 yields correct spin multiplicities for all ten TMCs, with the exception of TMC **10.** Here, erroneously the electronic ground state in solution is the low-spin state, whereas in the gas phase it is the high-spin state (Table 3). Hence, the parameter **$â_0 = 0.12$** was chosen for the B4LYP functional.

4.1.1 Spin multiplicity in dielectric medium

The energy splitting between low- and high-spin states in vacuum is defined as

$$\Delta G^\circ_{g,LS/HS} = G^\circ_{g,HS} - G^\circ_{g,LS} \qquad (4.1)$$
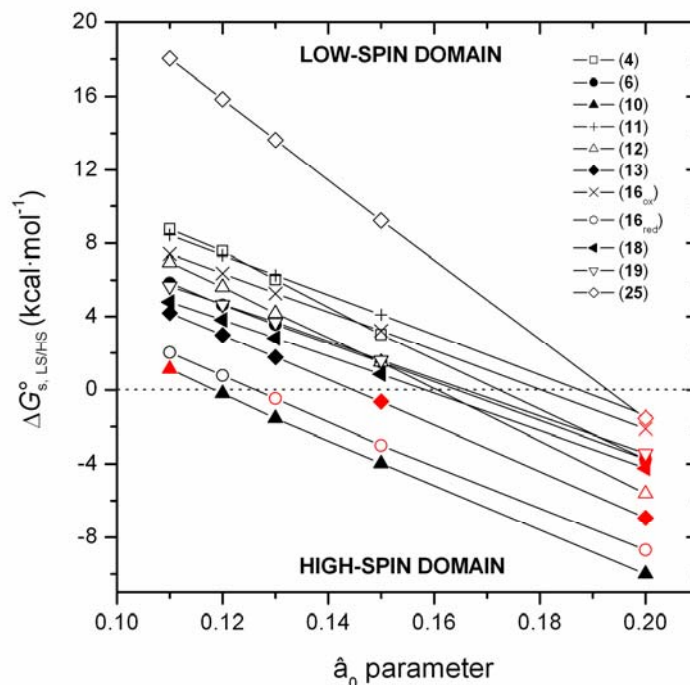
and in condensed phase as

$$\Delta G^\circ_{s,LS/HS} = G^\circ_{s,HS} - G^\circ_{s,LS} , \qquad (4.2)$$

where $G^\circ_{g,LS}$, $G^\circ_{g,HS}$, $G^\circ_{s,LS}$ and $G^\circ_{s,HS}$ are the low- and high-spin state free energies in vacuum and condensed phase, respectively.

The linear dependence of the energy splitting ($\Delta G^\circ_{g,LS/HS}$ and $\Delta G^\circ_{s,LS/HS}$) from the exact exchange parameter reported earlier by Reiher et al.[21] is nicely observed also from the results of the present study (Figure 22, Figure 23). Comparison of the dependencies $\Delta G^\circ_{g,LS/HS}$ (Figure 22) and $\Delta G^\circ_{s,LS/HS}$ (Figure 23) on the parameter $â_0$, demonstrates clearly the influence of the dielectric medium on the energy difference between low- and high-spin states. In the environment with dielectric constant of $\varepsilon > 1$ the electronic ground state multiplicity of the TMCs can change to both low- or high-spin (compare Figure 22 and Figure 23). The magnitude of this effect differs from compound to compound and in the case of TMCs considered in this work, obtains values of up to 39.9 kcal·mol^{-1} (**25**) . Therefore this influence cannot be neglected. Moreover, in many cases the predicted ground state multiplicities agree with experiment only after considering the effect of the dielectric medium (see Figures 22, 23 and Table 3). From equations (3.2), (4.1) and (4.2) follows, that the difference between $\Delta G^\circ_{s,LS/HS}$ and $\Delta G^\circ_{g,LS/HS}$ is nothing else than the difference in solvation energies between both spin states $\Delta\Delta G^\circ_{sol,LS/HS}$
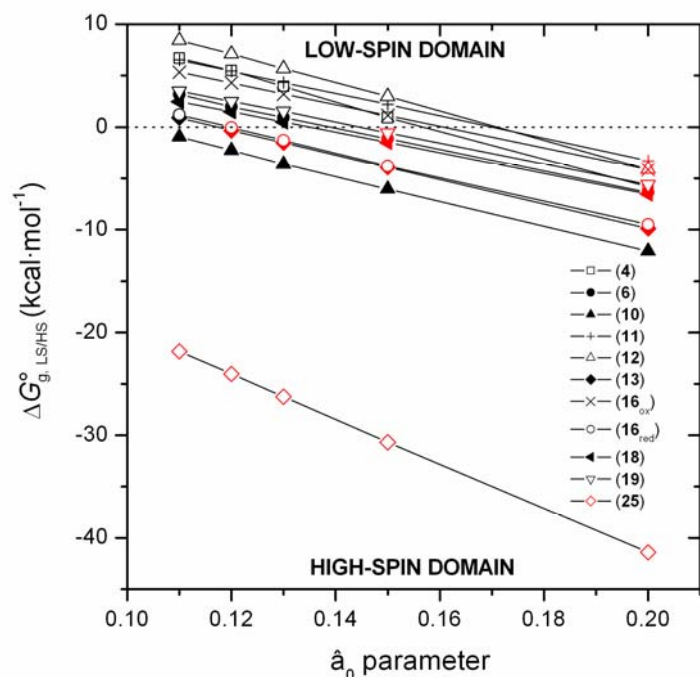
Figure 22. Energy splitting between high- and low-spin states of selection of TMC $\Delta G^{o}_{g,LS/HS}$ in vacuum, depending on the parameter $\hat{a}_0$ of exact exchange in the B4LYP functional [eq. (3.6)]. The other parameters in eq. (3.6) are fixed at values $a_0 = 0.20$, $a_x = 0.72$ and $a_c = 0.81$. Incorrectly reproduced ground state multiplicities are denoted by red symbols.

Figure 23. Energy splitting between high- and low-spin states of of selection of TMC $\Delta G^{o}_{s,LS/HS}$ in the condensed phase, depending on the parameter $\hat{a}_0$ of exact exchange in the B4LYP functional [eq. (3.6)]. The other parameters in eq. (3.6) are fixed at values $a_0 = 0.20$, $a_x = 0.72$ and $a_c = 0.81$. Incorrectly reproduced ground state multiplicities are denoted by red symbols. Since the difference between appropriate $\Delta G^{o}_{s,LS/HS}$ values for compound **4** in the water, acetonitrile and dimethylformamide is insignificant, for clearness, only the values in water are plotted on the graph.

$$\Delta G^{\circ}_{s,LS/HS} - \Delta G^{\circ}_{g,LS/HS} = \Delta G^{\circ}_{sol,HS} - \Delta G^{\circ}_{sol,LS} = \Delta\Delta G^{\circ}_{sol,LS/HS} , \qquad (4.3)$$

where $\Delta G^{\circ}_{sol,LS}$ and $\Delta G^{\circ}_{sol,HS}$ are solvation energies of TMC in low- and high-spin states, respectively.

For the compounds studied here in most of the cases a destabilization of the high-spin state in the condensed phase (see $\Delta\Delta G^{\circ}_{sol,LS/HS}$ values in the Table A9 of appendix) was observed. Hence, the question arises, what are the reasons for such a behavior. Obviously, the factors influencing the $\Delta\Delta G^{\circ}_{sol,LS/HS}$ are structure and charge distribution, which change by the alteration of the spin state. It is possible to determine the contributions from both factors to the $\Delta\Delta G^{\circ}_{sol,LS/HS}$ separately, by combining the partial charges and structures of low- and high-spin states independently, as described in the following. Let us consider the solvation energies for the three following cases (see Figure 24):

1. (LS^{structure};LS^{charge}) – with the structure optimized for low-spin state and partial charges generated for low-spin state (solvation energy $\Delta G^{\circ}_{sol,LS}$);

2. (HS^{structure};HS^{charge}) – with the structure optimized for high-spin state and partial charges generated for high-spin state (solvation energy $\Delta G^{\circ}_{sol,HS}$);

3. (HS^{structure};LS^{charge}) – with the structure optimized for high-spin state and partial charges generated for low-spin state (fictitious solvation energy $\Delta G^{\circ}_{sol,(HS;LS)}$).

In further discussion for convenience the short notations (LS;LS), (HS;HS), and (HS;LS) will be used, instead of (LS^{structure};LS^{charge}), (HS^{structure};HS^{charge}) and (HS^{structure};LS^{charge}), respectively.
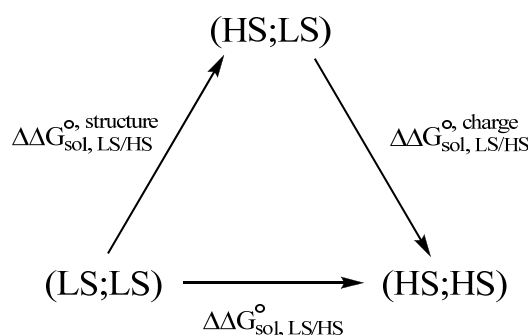
Figure 24. Thermodynamic cycle connecting (LS;LS), (HS;HS) and (HS;LS) states.

Note, that similarly to (HS;LS) the (LS;HS) state (combination of the structure optimized for low-spin state with the partial charges from the high-spin state) can be used alternatively. For our discussion, however, it is enough to use only one of these two fictitious cases. Arbitrarily, the (HS;LS) state was chosen. Additionally, the solvation energy of the (LS;HS) state ($\Delta G^{\circ}_{\mathrm{sol,(LS;HS)}}$) are given in the Table A9 of the appendix.

Via the fictitious (HS;LS) state, two real (LS;LS) and (HS;HS) states can be connected. These states are energetically coupled (Figure 24), so that $\Delta\Delta G^{\circ}_{\mathrm{sol,LS/HS}}$ can be given as

$$\Delta\Delta G^{\circ}_{\mathrm{sol,LS/HS}} = \Delta\Delta G^{\circ,\mathrm{structure}}_{\mathrm{sol,LS/HS}} + \Delta\Delta G^{\circ,\mathrm{charge}}_{\mathrm{sol,LS/HS}} , \tag{4.4}$$

where

$$\Delta\Delta G^{\circ,\mathrm{structure}}_{\mathrm{sol,LS/HS}} = \Delta G^{\circ,\mathrm{(HS;LS)}}_{\mathrm{sol}} - \Delta G^{\circ,\mathrm{(LS;LS)}}_{\mathrm{sol}} , \tag{4.5}$$

$$\Delta\Delta G^{\circ,\mathrm{charge}}_{\mathrm{sol,LS/HS}} = \Delta G^{\circ,\mathrm{(HS;HS)}}_{\mathrm{sol}} - \Delta G^{\circ,\mathrm{(HS;LS)}}_{\mathrm{sol}} . \tag{4.6}$$

While $\Delta\Delta G^{\circ,\mathrm{structure}}_{\mathrm{sol,LS/HS}}$ includes the contributions due to the structural differences of two spin states, the $\Delta\Delta G^{\circ,\mathrm{charge}}_{\mathrm{sol,LS/HS}}$ results from the alterations in the charge distribution. Analysis of data in the Table A9 of appendix shows no obvious correlation between the values of $\Delta\Delta G^{\circ,\mathrm{structure}}_{\mathrm{sol,LS/HS}}$ and $\Delta\Delta G^{\circ,\mathrm{charge}}_{\mathrm{sol,LS/HS}}$. It seems, that the observed preference to destabilize the high spin state in the dielectric medium is rather accidental.

While $\Delta\Delta G^{\circ,\mathrm{charge}}_{\mathrm{sol,LS/HS}}$ depends only on the charge distribution in the low- and high-spin states, two factors are contributing to the value of $\Delta\Delta G^{\circ,\mathrm{structure}}_{\mathrm{sol,LS/HS}}$. In the high spin state, the electrons of the transition metal occupy the d-orbitals (t_{2g}-orbitals by the octahedral and e_g-orbitals by the tetrahedral geometries), which are oriented towards the orbitals of the ligands. The repulsion between these orbitals leads to an increase of the metal-ligand distances and therefore to spacial expansion of the high-spin complex. Due to the volume enlargement of the compound in the high-spin state, the charge density of the transition metal complex decreases, compared to the low-spin state. As a consequence, the solvation energy of the high-spin TMCs is higher than in the low-spin state, resulting in the positive value of $\Delta\Delta G^{\circ,\mathrm{structure}}_{\mathrm{sol,LS/HS}}$. However this factor is effective only for the symmetric compounds possessing a dipole moment close to zero. Especially pronounced is this effect in case of the highly charged $[Fe(CN)_6]^{4-}$ (**1**) and $[Mn(CN)_6]^{4-}$ (**25**) complexes. For the non-symmetric TMCs the dipole moment becomes the

dominant factor influencing the value of $\Delta\Delta G_{\mathrm{sol,LS/HS}}^{\circ,\mathrm{structure}}$. The dipole moment itself depends not only on the structure, but also on the partial charges. Respectively, $\Delta\Delta G_{\mathrm{sol,LS/HS}}^{\circ,\mathrm{structure}}$ can obtain positive as well as negative values dependent on the charge distribution of both spin-states.

4.2 Determination of G_X term in B4(XQ3)LYP-approach

To determine the correction term $G_X(q)$ one assumes that it can be expressed as third-order polynomial in the total charge of the reduced state of the TMC

$$G_X(q) = \mathrm{A}q^3 + \mathrm{B}q^2 + \mathrm{C}q + \mathrm{D} . \tag{4.7}$$

Since only one-electron reduction processes are considered in present study the total charges of the reduced (q_{Red}) and oxidized (q_{Ox}) states obey $q_{\mathrm{Ox}} = q_{\mathrm{Red}} + 1$. Hence, $\Delta G_X = G_X(q_{\mathrm{Red}}) - G_X(q_{\mathrm{Ox}})$ can be expressed as

$$\Delta G_X(q_{\mathrm{Red}}) = -\mathrm{A}(3q_{\mathrm{Red}}^2 + 3q_{\mathrm{Red}} + 1) - \mathrm{B}(2q_{\mathrm{Red}} + 1) - \mathrm{C} . \tag{4.8}$$

Note that in the above difference the constant term D cancels. The remaining polynomial coefficients A, B and C in eq. (4.8) were determined via the following two-step fitting procedure, for which the compounds of the training set only (see Table 1) were used:

initialisation - To initialize the procedure, the $\Delta G_{\mathrm{g}}^{\circ, \mathrm{B4LYP}}$ [eq. (3.7)] and $\Delta\Delta G_{\mathrm{sol}}^{\circ}$ [eq. (3.3)] were calculated, where the latter were computed using in zero order approximation the same set of atomic radii (Bondi radii[129]) for all three solvents considered. These energies enter the free energy of reduction as follows

$$\Delta G_{\mathrm{s}}^{\circ} = \Delta G_{\mathrm{g}}^{\circ, \mathrm{B4LYP}} + \Delta\Delta G_{\mathrm{sol}}^{\circ} + \Delta G_X(q_{\mathrm{Red}}) . \tag{4.9}$$

1-st step - for fixed values of $\Delta G_{\mathrm{g}}^{\circ, \mathrm{B4LYP}}$ and $\Delta\Delta G_{\mathrm{sol}}^{\circ}$, the redox potentials obtained from G_{s}°, eq. (4.9), were matched with the measured values, by adjusting the parameters of $\Delta G_X(q_{\mathrm{Red}})$, eq. (4.8), using the averages $\langle \Delta G_X(q_{\mathrm{Red}}) \rangle$ of TMCs with the same charge q_{Red} in a least square fit of the polynomial coefficients in $G_X(q_{\mathrm{Red}})$ with the program Origin 7.5.[135]

2-nd step - for fixed $\Delta G_X(q_{\mathrm{Red}})$, the $\Delta\Delta G_{\mathrm{sol}}^{\circ}$ were reevaluated to improve the agreement with the measured redox potentials, by varying the atomic radii. For different solvents different values of atomic radii were used.

   Then, one returns back to step **1** to reevaluate $\Delta G_X(q_{\mathrm{Red}})$ for fixed $\Delta\Delta G_{\mathrm{sol}}^{\circ}$ and so forth. The optimization procedure was repeated until the
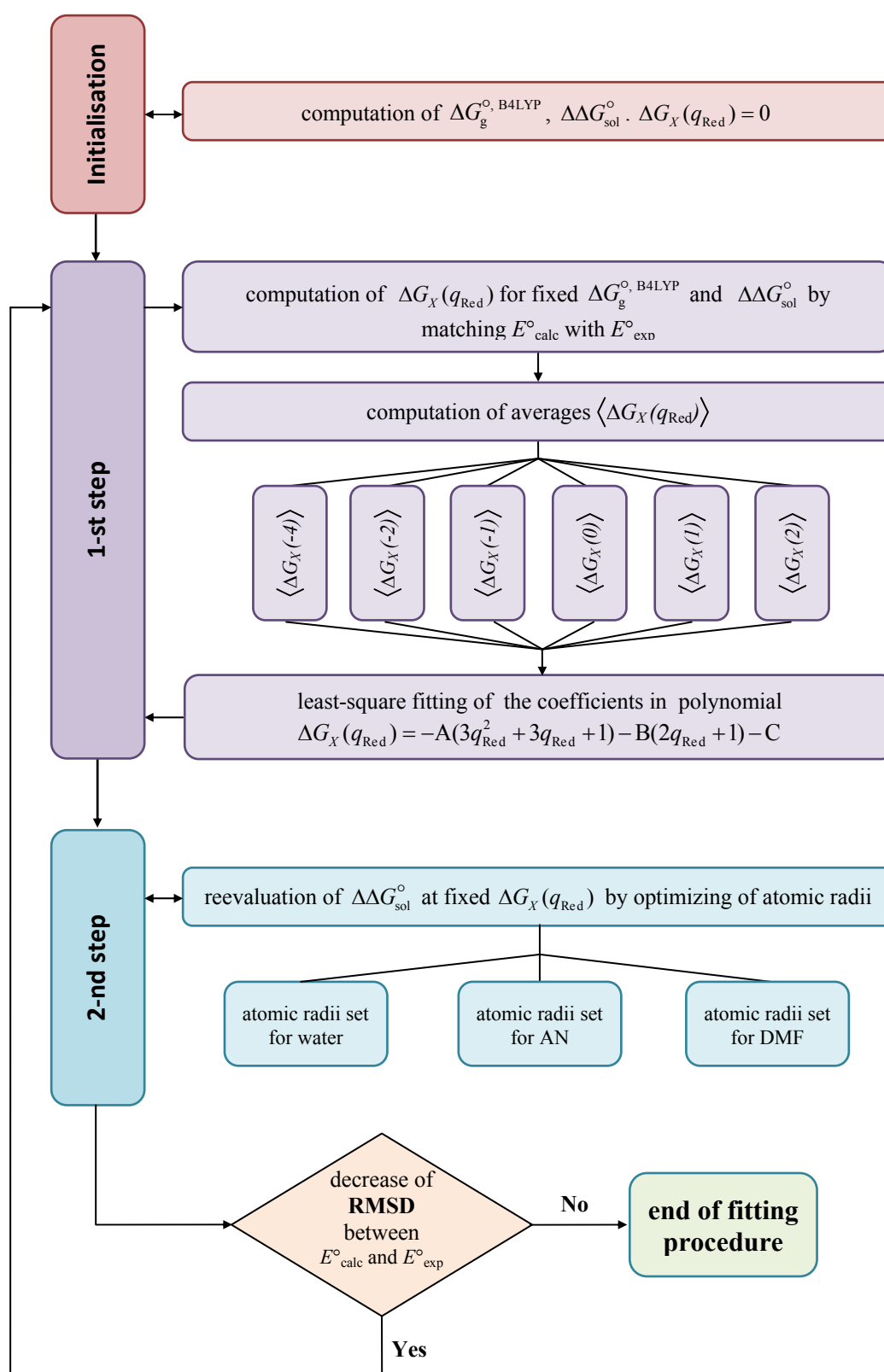
Figure 25. Flowchart of the fitting procedure used to obtain the coefficients in the eq. (4.8)

RMSD between calculated and measured redox potentials did not decrease anymore.

The flowchart of the described fitting procedure is shown on the Figure 25. The fitting procedure yields the following values for the coefficients in eq. (4.8): A = −0.333, B = 1.545 and C = 21.634 in units of kcal·mol^{-1}. The corresponding polynomial $\Delta G_X(q_{Red})$ is given in the Figure 26. It is used to the calculate the post-computational correction G_X in eq. (3.7), which is required for the evaluation of redox potentials.
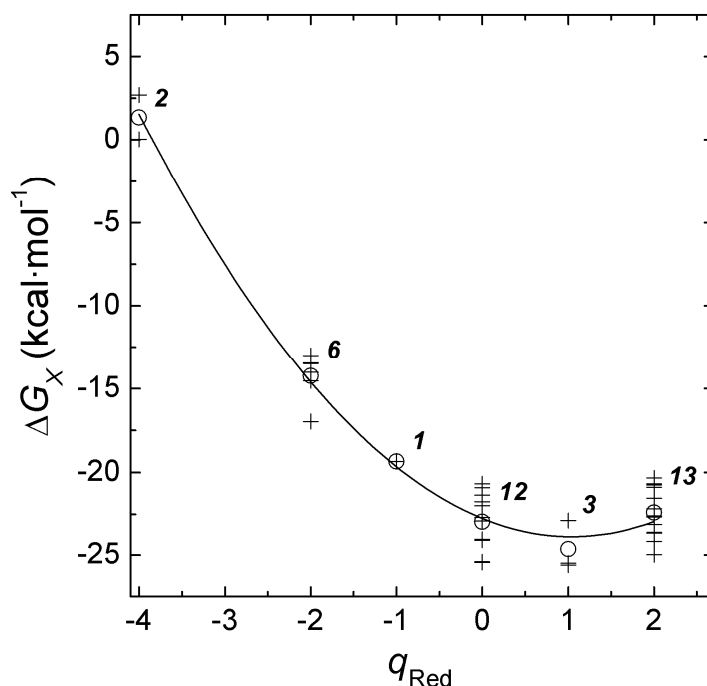
Figure 26. The $\Delta G_X(q_{Red})$ polynomial fitted to the mean values $\langle \Delta G_X(q_{Red}) \rangle$ (open circles). For the fit procedure the complexes 1-12 and 14-30 were used. Individual $\Delta G_X(q_{Red})$ values are displayed by crosses. The fitted parameters in Eq. (4.8) are A = −0.333, B = 1.545 and C = 21.634. Numbers in the plot refer to the number of measured redox potentials for different TMCs and solvents available at a specific q_{Red}. The charges are given in dimensionless units of the elementary charge.

From the non-linear plot in Figure 26 it becomes evident that at least a third-order polynomial is required.

For each solvent a different set of atomic radii was used, as explained in paragraph 3.1.6. The values of the optimized atomic radii are given in Table 4. For the aprotic solvents acetonitrile and dimethylformamide the atomic radii have to be considerably larger than for water, a protic solvent. This is in agreement with prior work[14, 128]. The smaller atomic radii for the protic solvents were explained to be necessary to account for the stronger interaction of the solute with the polar hydrogens of the protic

solvent[14]. The explanation of small differences in atomic radii between the two aprotic solvents is more subtle.

Table 4. Optimized atomic radii for different solvents in comparison to Bondi radii[129].

atom	atomic radii, Å			
	water	AN[a]	DMF[a]	Bondi
H	1.00	1.00	1.17	1.20
C	1.65	1.80	1.85	1.70
N	1.60	1.76	1.76	1.55
O	1.60	1.76	1.76	1.52
S	1.71	2.18	2.20	1.75
Cl	–	1.76	2.05	1.80

[a] AN: acetonitrile; DMF: dimethylformamide.

4.3 Redox potentials. Theory versus experiment.

The results of redox potential calculation for the training set of TMCs (Table 1), using the B4(XQ3)LYP-approach are demonstrated in Figure 27, where 38 calculated redox potentials are plotted against the corresponding experimental values. For these redox potentials the calculated and experimental values correlate very well yielding RMSD = 68 mV and a mean absolute deviation (MAD) of 58 mV. The maximum absolute deviation of 148 mV was observed for compound **13**.
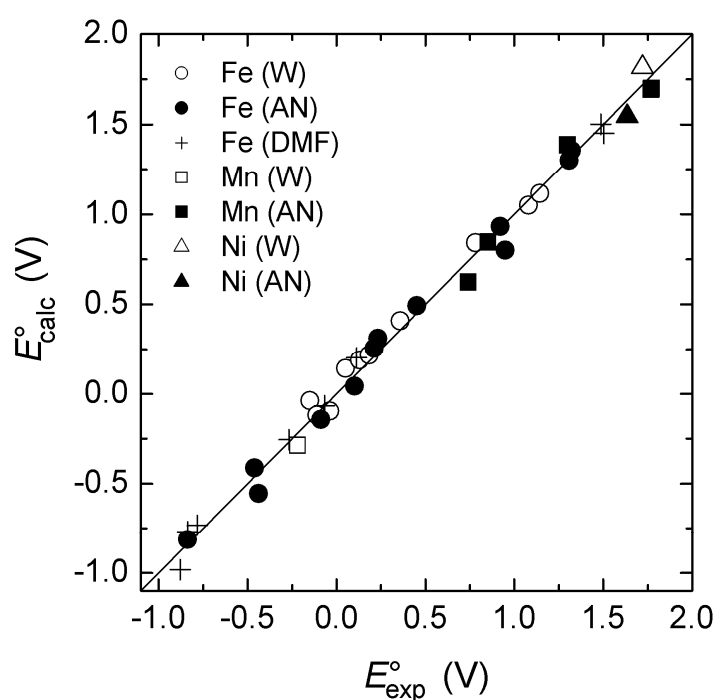
Figure 27. Correlation between calculated and measured redox potentials of the training set (Table 1). Redox potentials were calculated for 38 redox potentials of 30 different transition metal compounds using the B4(XQ3)LYP-approach. RMSD = 68 mV, MAD = 58 mV.

Such a large deviation could be due to the fact that the exact structures of the redox states in solution are missing. Instead of them, one uses the geometries optimized in vacuum, under assumption that structural changes occuring by transferring the TMC from the vacuum into the solvent are small enough to be neglected. This assumption might not always be correct. Excluding compound **13** the RMSD reduces to 65 mV (MAD = 55 mV). According to results obtained with the B4(XQ3)LYP-approach the procedure works surprisingly well. It provides the equally good agreement for iron,

manganese and nickel TMCs, although, the method was developed originally only for iron metal complexes. For these three transition metals a single parameter set of the correction term $G_X(q)$ is sufficient to reproduce redox potentials reliably. However, it is possible that an individual parameterization of the B4(XQ3)LYP-approach for each type of transition metal might give even better results.
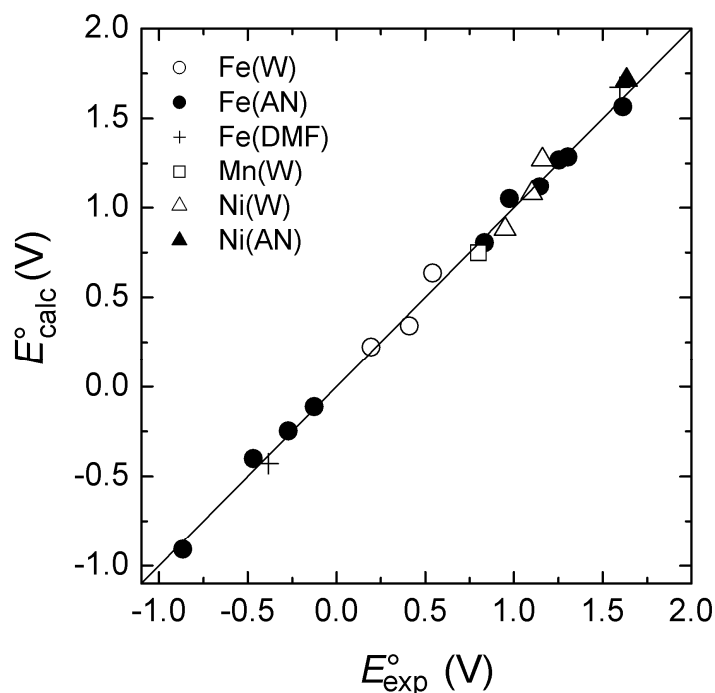
Figure 28. Correlation between calculated and measured redox potentials for the prediction set (Table 2). Redox potentials were calculated for 20 redox potentials of 18 different transition metal compounds using the B4(XQ3)LYP-approach. RMSD = 57 mV, MAD = 50 mV.

The reliability of the B4(XQ3)LYP-approach was demonstrated by applying it for the calculation of the redox potentials of TMCs in the prediction set (Table 2). In that case (see Figure 28) the B4(XQ3)LYP-approach shows very good performance, with an RMSD of 57 mV (MAD = 50 mV), confirming the quality of the parameters gained the training set. The RMSD for both training and prediction sets together is 65 mV (MAD = 55 mV). The comparison of results obtained from the B4(XQ3)LYP-approach with those obtained from B3LYP (Tables 5 and 6) demonstrates clearly the superiority of the B4(XQ3)LYP-approach (Figure 29). Despite a strong correlation of the measured redox potentials with results computed with the B3LYP functional the deviations are considerably larger (RMSD = 183 mV, MAD = 127 mV and a maximal deviation of 464 mV) (Figure 30, Tables 5-6). Nevertheless, the MAD value (127 mV) is still 23 mV less than obtained in previous computations[2] using the same level of theory (B3LYP/LACV3P**++) for TMCs. This shows clearly that our electrostatic approach

(involving specific values of atomic radii and charges), although optimized for the B4(XQ3)LYP-approach, also works well in combination with the B3LYP functional. In fact, the absolute redox potentials calculated with B3LYP are generally underestimated (Figure 30). Hence, adding 90 mV to the computed redox potentials reduces the RMSD from 183 mV to 162 mV (Figure 31). For comparison, the RMSD reported for calculated redox potentials of 270 different organic compounds involving similar corrections is 170 mV[12].
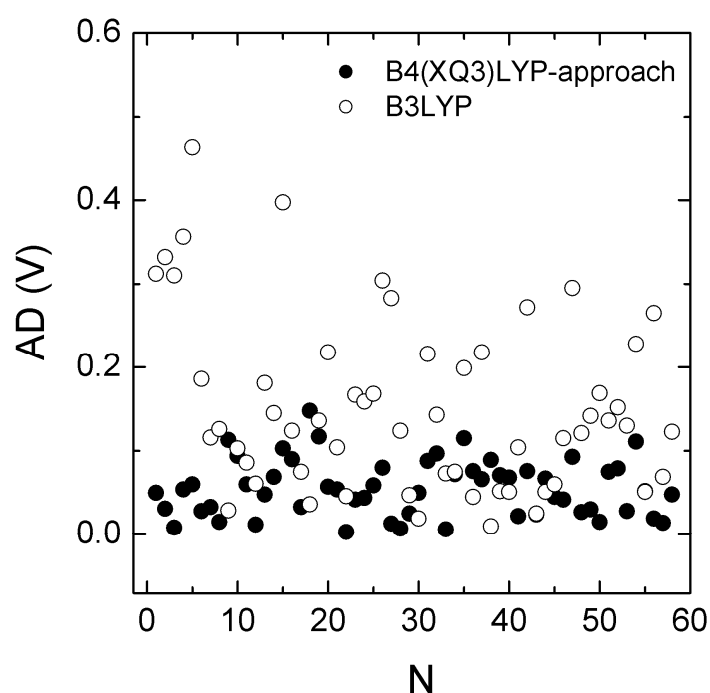
Figure 29. Absolute deviations (AD) between calculated (using B4(XQ3)LYP and B3LYP) and measured redox potentials considering all 58 values in Tables 1 and 2. N refers to the sequence of redox potentials as listed in Tables 1 and 2.

Table 5. Redox potentials versus SHE [V] calculated for the training set using B3LYP, B4(XQ3)LYP-approach and experimental redox potentials of the model compounds in different solvents. Where multiple experimental redox potentials are available, the mean values were considered (given in parenthesis). The considered solvents are water, acetonitrile (AN) and dimethylformamide (DMF). Redox potentials reported originally for different reference electrodes were converted to SHE by adding the following constants: *SCE* +0.244 V[78], *Fc+/Fc in AN* +0.624 V[78], *Fc+/Fc in DMF* +0.702 V[85], *Ag/AgCl* +0.200 V[84]. Using the B3LYP DFT functional to compute redox potentials, the electronic states of lowest energy obtained in the computations were considered, regardless of the nature of the measured spin multiplicity.

	substance	solvent	E°_{calc} (B3LYP)	E°_{calc} (B4(XQ3)LYP-approach)	E°_{exp}
1.	$[Fe(CN)_6]^{3-/4-}$	water	0.670	0.408	0.358[127]
2.	$[Fe(bpy)_3]^{3+/2+}$	water	0.748	1.049	1.030[127], 1.089[136], 1.120[137] (1.080)
		AN	0.999	1.301	1.322[138], 1.304[139], 1.302[140] (1.309)
		DMF	1.148	1.450	1.504[141]
3.	$[Fe(bpy)_2(CN)_2]^{1+/0}$	water	0.318	0.842	0.782†
4.	$[Fe(phen)_3]^{3+/2+}$	water	0.958	1.116	1.147[127], 1.141[137] (1.144)
		AN	1.206	1.355	1.322[139]
		DMF	1.361	1.502	1.487[141]
5.	$[Fe(diammac)]^{3+/2+}$	water	-0.180	-0.038	-0.150[142]
6.	$[Fe(sar)]^{3+/2+}$	water	0.152	0.143	0.050[142]
7.	$[Fe(tacn)_2]^{3+/2+}$	water	0.216	0.190	0.130[117]
8.	$[Fe(PyIm_2H_2)_2]^{3+/2+}$	AN	0.981	0.932	0.920[106]
9.	$[Fe(PyIm_2)_2]^{1-/2-}$	AN	-0.641	-0.412	-0.460[106]
10.	$[Fe(PypepO)_2]^{1-/2-}$	DMF	-0.983	-0.769	-0.838[109]
11.	$[Fe(PypepS)_2]^{1-/2-}$	DMF	-1.275	-0.981	-0.878[110]
12.	$[Fe(PyAS)_2]^{1+/0}$	DMF	-0.012	0.202	0.112[110]
13.	$[Fe(bpteta)]^{3+/2+}$	AN	0.913	0.801	0.949[101]
14.	$[Fe(DITim)_2]^{1+/0}$	AN	-0.574	-0.555	-0.438[107]
15.	$[Fe(Pypep)_2]^{1+/0}$	water	-0.256	-0.122	-0.038[114]
		AN	-0.192	-0.142	-0.088[114]
		DMF	-0.114	-0.065	-0.068[114]
16.	$[Fe(Prpep)_2]^{1+/0}$	water	0.109	0.217	0.184[105]
17.	$[Fe(PaPy_3)(AN)]^{2+/1+}$	AN	0.285	0.494	0.452[113]
18.	$[Fe(PaPy_3)(Cl)]^{1+/0}$	AN	0.053	0.259	0.212[113]
19.	$[Fe(PaPy_3)(N_3)]^{1+/0}$	AN	-0.066	0.043	0.102[113]
20.	$[Fe(PaPy_3)(CN)]^{1+/0}$	AN	-0.072	0.312	0.232[113]
21.	$[Fe(PaPy_2O)(Cl)]^{0/1-}$	DMF	-0.551	-0.255	-0.268[109]
22.	$[Fe(SEt)_4]^{1-/2-}$	AN	-0.885	-0.813	-0.838[108]
23.	$[Fe(S_2-o-xyl)_2]^{1-/2-}$	DMF	-0.802	-0.733	-0.783[119]
24.	$[Fe(SEtOH)_4]^{1-/2-}$	water	-0.234	-0.117	-0.110[116]
25.	$[Mn(CN)_6]^{3-/4-}$	water	-0.002	-0.286	-0.220[127]
26i.	$[Mn(bpia)(Cl)_2]^{1+/0}$	AN	0.779	0.846	0.852[115]
26ii.	$[Mn(bpia)(Cl)_2]^{2+/1+}$	AN	1.697	1.700	1.772[115]
27i.	$[Mn(py_2(NMe)_2Cl_2)]^{1+/0}$	AN	0.541	0.625	0.740[100]
27ii.	$[Mn(py_2(NMe)_2Cl_2)]^{2+/1+}$	AN	1.725	1.694	1.770[100]
28.	$[Mn(bpteta)]^{3+/2+}$	AN	1.515	1.387	1.299[101]
29.	$[Ni(bpy)_3]^{3+/2+}$	water	1.863	1.817	1.720[143]
30.	$[Ni(bpteta)]^{3+/2+}$	AN	1.624	1.545	1.634[101]

†-extrapolated using data from [144].

Table 6. Redox potentials versus SHE [V] calculated for the prediction set using B3LYP, B4(XQ3)LYP-approach and experimental redox potentials of the model compounds in different solvents. Where multiple experimental redox potentials are available, the mean values were considered (given in parenthesis). The considered solvents are besides water AN=acetonitrile and DMF=dimethylformamide. Redox potentials reported originally for different reference electrodes were converted to SHE by adding the following constants: *SCE* +0.244 V[78], *Fc+/Fc in AN* +0.624 V[78], *Fc+/Fc in DMF* +0.702 V[85], *Ag/AgCl* +0.200 V[84]. Using the B3LYP DFT functional to compute redox potentials, the electronic states of lowest energy obtained in the computations were considered, regardless of the nature of the measured spin multiplicity.

	substance	solvent	E°_{calc} (B3LYP)	E°_{calc} (B4(XQ3)LYP-approach)	E°_{exp}
31[i].	[Fe(cyclamAc)(N$_3$)] $^{2+/1+}$	AN	1.491	1.566	1.614[145]
31[ii].	[Fe(cyclamAc)(N$_3$)] $^{1+/0}$	AN	-0.057	-0.112	-0.126[145]
32.	[Ni(tacn)]$^{3+/2+}$	water	1.002	0.879	0.950[117]
33.	[Fe(dtne)]$^{3+/2+}$	water	0.461	0.342	0.410[146]
34.	[Ni(dtne)]$^{3+/2+}$	water	1.204	1.078	1.100[146]
35.	[Fe(terpy)$_2$]$^{3+/2+}$	DMF	1.325	1.673	1.597[141]
36.	[Fe(SPh)$_4$]$^{1-/2-}$	AN	-0.296	-0.247	-0.271[108]
37.	[Fe(SCH$_2$CON(CH$_3$)$_2$)$_4$]$^{1-/2-}$	AN	-0.417	-0.401	-0.468[104]
		DMF	-0.444	-0.429	-0.384[104]
38.	[Fe(S-*i*-Pr)$_4$]$^{1-/2-}$	AN	-0.981	-0.908	-0.866[108]
39.	[Fe(bpy)(CN)$_4$]$^{3+/2+}$	water	0.247	0.635	0.542[137]
40.	[Fe(tacnPy$_2$)(AN)]$^{3+/2+}$	AN	1.025	1.119	1.146[112]
41.	[Fe(N$_4$Py)(Cl)]$^{2+/1+}$	AN	0.692	0.804	0.834[111]
42.	[Fe(N$_4$Py)(AN)]$^{3+/2+}$	AN	1.085	1.269	1.254[111]
43.	[Fe(Py$_3$tacn)]$^{3+/2+}$	AN	0.838	1.049	0.974[118]
44.	[Ni(Py$_3$tacn)]$^{3+/2+}$	AN	1.786	1.713	1.634[118]
45.	[Fe(TCTA)]$^{0/1-}$	water	0.065	0.223	0.195[147]
46.	[Ni(TCTA)]$^{0/1-}$	water	1.388	1.271	1.160[147]
47.	[Mn(TCTA)]$^{0/1-}$	water	0.851	0.748	0.800[147]
48.	[Fe(Pyr$_2$Py)$_2$]$^{3+/2+}$	AN	1.039	1.285	1.304[148]
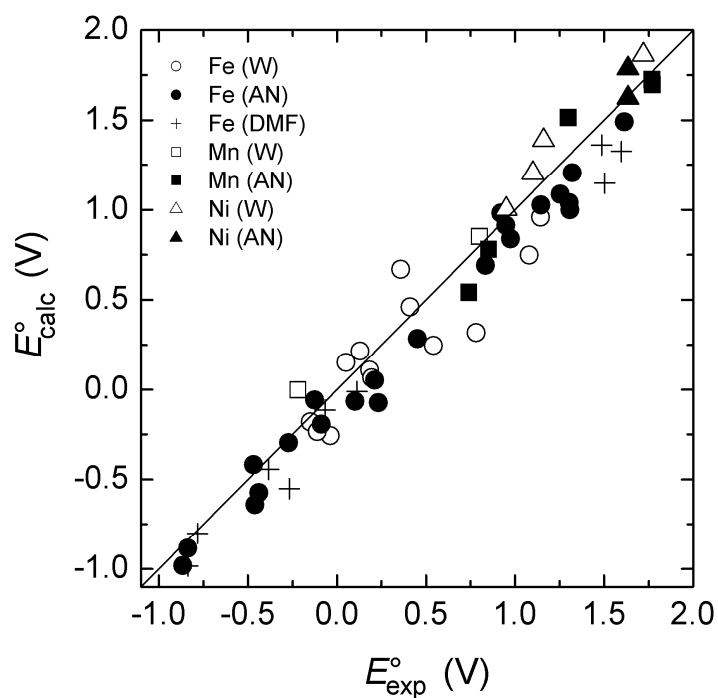
Figure 30. Correlation between calculated and experimental redox potentials for the training and prediction sets. Redox potentials are calculated using B3LYP. RMSD = 183 mV, MAD = 127 mV
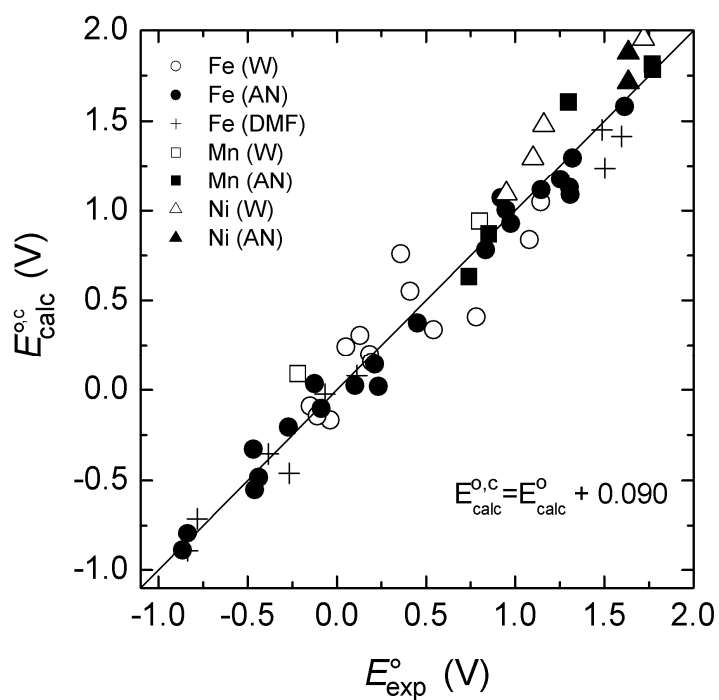
Figure 31. Calibrated correlation between calculated and experimental redox potentials for the training and prediction sets. Redox potentials are calculated using B3LYP. Originally calculated redox potentials E_{calc}^{o} were corrected by adding 90 mV to get calibrated redox potentials $E_{calc}^{o,c}$.

4.4 Computational costs

The CPU-time is an important issue for prospective users of the B4(XQ3)LYP-approach. It is difficult to give here exact numbers, since many factors can influence CPU-time (number of atoms, basis sets, type of calculation and quantum-chemical software used, type of CPU and memory of the computer, etc.). The time limiting part here is generally the quantum chemistry. Compared to the quantum chemical computations, the time which is needed for the electrostatic calculations is negligible (typically some minutes). Examples are given in the Table 7 to get a general idea of how expensive the quantum-chemical computations in B4(XQ3)LYP-approach are for different cases. The data presented in the Table 7 are related to the values obtained from the computations using the quantum-chemical package Jaguar 5.0[122], which proceeds much faster than many others conventional *ab initio* programs, and is especially optimized for treating the systems containing TMCs.

Table 7. Detailed information on CPU-time needed to perform quantum-chemical computations within the B4(XQ3)LYP-approach for the systems of different molecular size using the program JAGUAR 5.0[122] on a single CPU.

Number of atoms	TMC	Spin state	1 CPU-time*, *hours*		Total 1 CPU-time**, *hours*
			optimization	frequency calculation	
13	**1.** $[Fe(CN)_6]^{3-}$	1/2	0.43	1.20	8.78
	1. $[Fe(CN)_6]^{3-}$	5/2	0.40	1.46	
	1. $[Fe(CN)_6]^{4-}$	0	0.33	0.83	
	1. $[Fe(CN)_6]^{4-}$	2	0.43	1.20	
48	**18.** $[Fe(PaPy_3)(Cl)]^{1+}$	1/2	8.00	58.94	273.87
	18. $[Fe(PaPy_3)(Cl)]^{1+}$	5/2	5.82	74.07	
	18. $[Fe(PaPy_3)(Cl)]^{0}$	0	0.40	1.46	
	18. $[Fe(PaPy_3)(Cl)]^{0}$	2	8.00	58.94	
67	**4.** $[Fe(phen)_3]^{3+}$	1/2	1.63	162	540.92
	4. $[Fe(phen)_3]^{3+}$	5/2	2.07	134.6	
	4. $[Fe(phen)_3]^{2+}$	0	0.92	83.75	
	4. $[Fe(phen)_3]^{2+}$	2	10.35	145.6	

* on the 64 bit 2.6 GHz Opteron 285 processor

** includes CPU-time of optimization and frequency calculation for the low- and high-spin states of both redox species.

Depending on the size of the TMC system the computations can take from some hours to up to several days on a single CPU (Table7). If the ground state multiplicities of the TMCs are unknown, the low- and high-spin states must both be calculated within the B4(XQ3)LYP-approach, which increases the computational costs. Most expensive are the frequency calculations (see Table 7) for getting zero-point vibrational energy and the termal vibrational energy at 298 K, $\Delta G_{0\rightarrow298K}$ (see Eq. (3.4)). The contributions of these values to the redox potential are essential (see Table A2), such that their computation cannot be avoided. However, it should not be a big problem in the near future, since the processor manufacturer are continually coming out with more powerfull and faster CPUs. Moreover, by using of parallel computing the real-time for the prediction of the redox potential can be essentially decreased. For example, the redox potential for the biggest TMC considered in this work, the 67 atom compound **4** can be obtained in 3.5 days by using 8 CPUs in parallel.

According to data given in Figure 19 the average number of atoms per compound is 48. According values in Table 7, for compound of that size redox potential can be computed in ~ 273.87 hours on a single CPU. Using this number it is possible to make a very rough estimate of the CPU-time spent for the redox potential computation of all considered in this study compounds together, which makes ~ 13146 hours.

4.5 Computation of the redox potential difference for non-heme iron model compounds in vacuum using B3LYP und B4(XQ3)LYP-approach

In this chapter an example is presented where the elements of B4(XQ3)LYP-approach were applied to characterize a transition metal cofactor in a protein. The system under investigation was the non-heme iron cofactor in bacterial photosynthetic reaction center (bRC) (Figure 32). The general scheme of the electron transfer in bRC is represented in Figure 33. In these reaction centers an electron is transferred from the special pair (P) via the accessory bacteriochlorophyll (B_A), the bacteriopheophytin (H_A) and the primary quinone (Q_A) to reach finally the secondary quinone (Q_B).
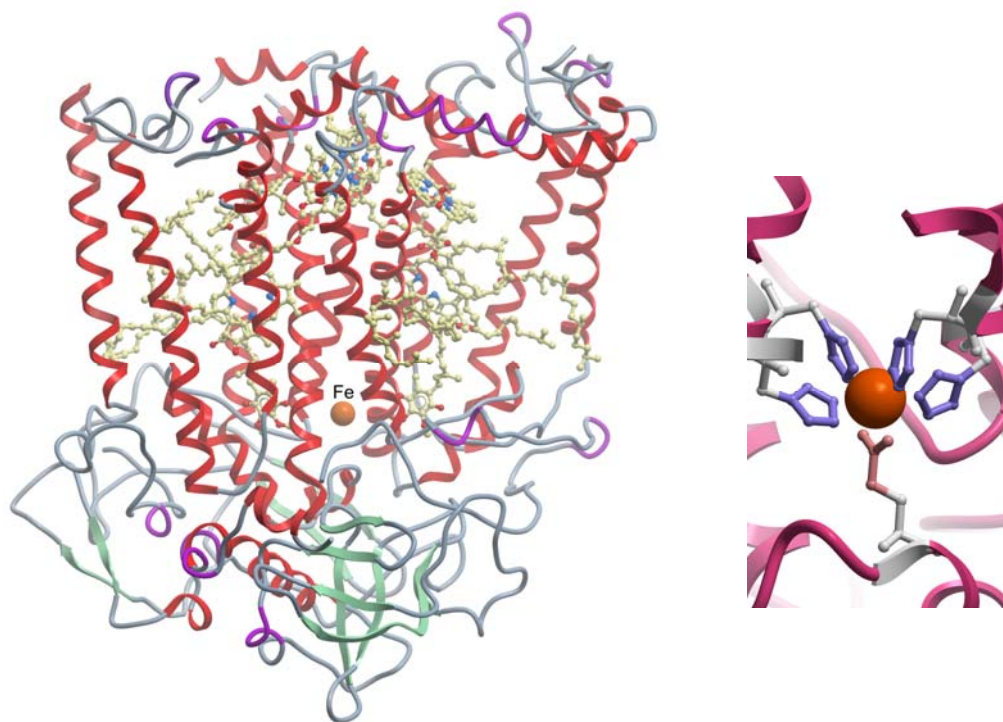
Figure 32. General (*left*) and detailed (*right*) views of the non-heme iron cofactor in photosynthetic bacterial reaction center of *Rhodobacter sphaeroides*. PDB code 1AIG[149].

In the electron transfer process between the two quinones Q_A and Q_B the role of the non-heme iron complex located between them is unclear. While some studies[150] indirectly suggested an involvement of the non-heme iron cofactor in this electron transfer process, others claimed the opposite[151]. Interestingly, the non-heme iron in the structurally similar photosystem II (PSII), is redox active although this is functionally not relevant. These conflicting views motivated to perform a computational study of the redox properties of non-heme iron complex in bRC by Ishikita et al.[152].

Normally such studies were done exclusively by using electrostatic energy computations[153, 154] combined with the knowledge of the measured redox potential of an analog model complex in a solvent. In this approach the electrostatic energy difference of the reduced and oxidized state of the cofactor is computed in the protein and solvent environment and the resulting difference of these electrostatic contributions to the redox energies is added the experimental redox potential of the model complex. This procedure works generally well since all other energy contributions approximately cancel in the double energy difference. However, for the non-heme iron complex no suitable model system in solution is available. Although in PSII the analog non-heme iron complex with measured E_{m}° exists, it is structurally slightly different and more importantly it possesses a different ligand composition. Hence, the procedure developed in the present work is a suitable alternative to calculate the redox potential of this type of cofactor both in bRC and PSII.
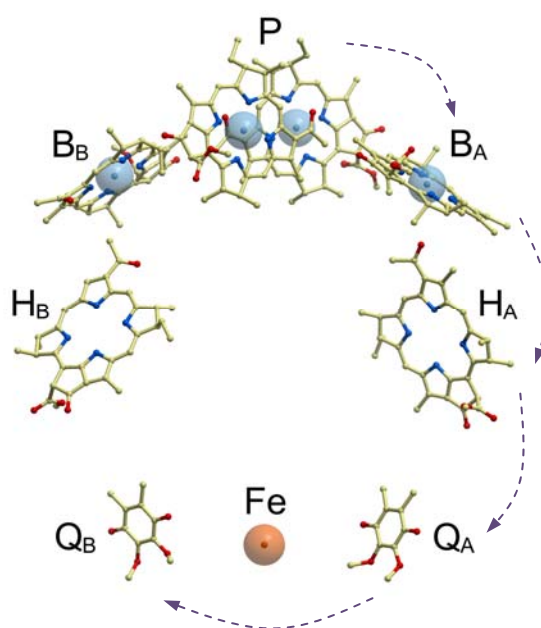
**Figure 33**. Electron transfer processes in bRC

The E_{m}° in bRC and PSII were estimated by computing the E_{m}° of suitable model complexes in vacuum ($E_{\mathrm{m}}^{\circ,\mathrm{vac}}$). For this purpose, the non-heme iron model compounds corresponding to those in bRC (Fe$_{\mathrm{model}}$bRC) and PSII (Fe$_{\mathrm{model}}$PSII) were considered. Both models were derived from the atomic coordinates of the WT-bRC crystal structure[149], which was subsequently geometry optimized. The information from the PSII crystal structure was not considered for two reasons. (i) The crystal structure of PSII is of lower resolution than of bRC. (ii) Geometry optimizations of the model

compounds that start from different initial coordinates may result in different energy minima.
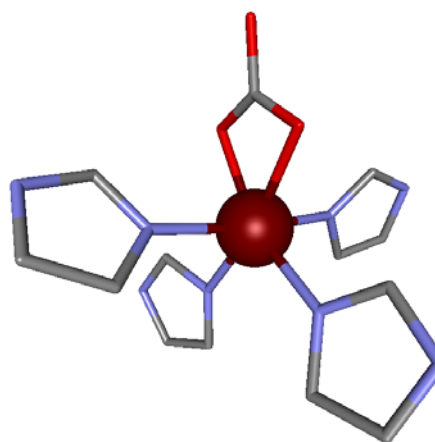
The redox potential difference in vacuum was calculated as

$$\Delta E_{\mathrm{m}}^{\circ,\mathrm{vac}} = E_{\mathrm{m}}^{\circ,\mathrm{vac}}([\mathrm{Fe_{model}bRC}]) - E_{\mathrm{m}}^{\circ,\mathrm{vac}}([\mathrm{Fe_{model}PSII}]), \qquad (4.10)$$

where the connection between redox potential and Gibbs free energy is defined by Eq. (3.4).
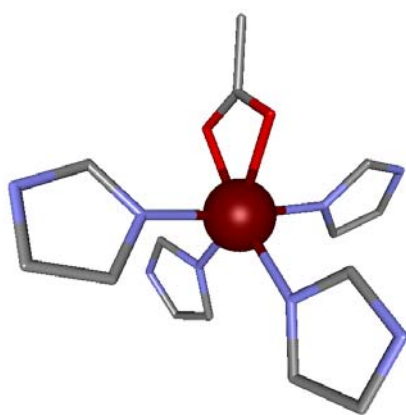
Figure 34. Model compound of non-hem iron in bRC

Figure 35. Model compound of non-hem iron in PSII

Both model structures ($Fe_{model}bRC$ and $Fe_{model}PSII$) include five ligands, which are four histidines and a carboxylic acid. The fifth bidentate ligand is a glutamate for bRC and a bicarbonate for PSII. The histidines were replaced by imidazoles the glutamate was substituted by acetate in bRC (Figure 34). This structure of $Fe_{model}bRC$ was then optimized according the procedure described in paragraph 3.1.3. Additionally, to avoid larger deviations from the atomic coordinates of the crystal structure all torsion angles were fixed such that only bond lengths and bond angles of $Fe_{model}bRC$ were optimized. In the quantum chemical computations, we considered the high spin states for the ferrous (S=2) and ferric (S=5/2) complexes. Based on the crystal structures of bRC and PSII the overlay of the atoms that are common for the two Fe model complexes yielded a RMSD of 0.32 Å. Relative to the initial model structure $Fe_{model}bRC$ from the bRC crystal the RMS deviation of the optimized reduced structure $[Fe_{model}bRC]^{1+}$ is 0.15 Å, while the RMS deviation is only 0.09 Å between optimized reduced $[Fe_{model}bRC]^{1+}$ and optimized oxidized $[Fe_{model}bRC]^{2+}$ geometries. The optimized structures of the redox states $[Fe_{model}bRC]^{1+}$ and $[Fe_{model}bRC]^{2+}$ were used to build up the starting structures of $[Fe_{model}PSII]^{1+}$ and $[Fe_{model}PSII]^{2+}$, respectively, where the methyl group of acetate was

replaced by an OH group in order to generate a bicarbonate (Figure 35). During the geometry optimization of the $Fe_{model}PSII$ model complexes all atoms except for the OH group were fixed.

Since the redox potential difference in vacuum was needed, only the quantum-chemical part of the B4(XQ3)LYP-approach, B4LYP, was used (see Eq. (3.6). By chance, the results obtained for $\Delta E_m^{\circ,vac}$ using B3LYP and B4LYP are identical giving -99 mV. Obviously an error compensation is taking place in the difference $\Delta E_m^{\circ,vac}$, including a double difference of energies. Such efficient error compensation was provided also by using the above described method of creating and optimizing the model compounds $Fe_{model}bRC$ and $Fe_{model}PSII$. The value of $\Delta E_m^{\circ,vac} = -99mV$ was further used by Ishikita et al (ref) for the calculation of the redox potential of the non-heme iron cofactor in bRC, which was obtained to be 186 mV[152].

By using structures of $Fe_{model}bRC$ and $Fe_{model}PSII$, which where obtained by optimizing the model complexes without restraining the torsion angles, no efficient error compensation in the difference $\Delta E_m^{\circ,vac}$ can be provided anymore, so that B3LYP and B4LYP lead to different values of $\Delta E_m^{\circ,vac}$, -134 mV and -73 mV, respectively.

4.6 Conclusion and outlook

The success of the B4(XQ3)LYP-approach for calculations of the absolute redox potentials of TMCs yielding an RMSD of 65 mV in comparison with experimental data is obvious. Indirectly it justifies our B4XLYP-hypothesis at least for the calculation of redox potentials of the considered TMCs. However, the exact form and the nature of the additional term E_x^X in the DFT functional is unknown. In this context the following questions arise:

1) Is the E_x^X term playing a general role in the DFT approach, improving not only the hybrid-GGA potentials, but also other LSDA- and GGA-type exchange-correlation potentials?

2) Is the E_x^X term specific only for the B3LYP functional?

3) If E_x^X really refers to a term of the DFT functional, is it contributing only to exchange or to correlation energy or is it simultaneously contributing to both energies?

4) Has E_x^X something to do with exchange-correlation or is it a pure empirical correction?

The only information that is available at the moment is the empirical post-computational simulation that mimics the influence of E_x^X for the redox potentials TMCs considered here. The post-computation is performed by the third-order polynomial $G_X(q)$ in the total charge that is parameterized using a number of TMCs. This is of course not enough to start with speculations on the nature of E_x^X and to answer the above mentioned questions. $G_X(q)$ probably does more than just compensation of E_x^X. It could also compensate for other possible deficiencies inherent in the DFT approach for TMCs. For example, the systematic underestimation of the redox-potentials occurring by using B3LYP (it could well be that this defect is also present in the incomplete B4LYP functional). In this sense, the information included in the $G_X(q)$ term can be considered as "contaminated". Extensions of the B4(XQ3)LYP-approach in the future, and studies on other model systems and other functionals will help to better understand the exact nature of the E_x^X term.

Knowing the exact form of the E_x^X term would in principle enable the DFT approach to be generally useful for a large class of compounds. However, without this knowledge one is restrained to employ an optimized post-computational correction function, which

is specialized to compute redox potentials of TMCs and could vary for different quantities and different types of compounds.

In its present form the B4(XQ3)LYP-approach can be applied to calculate redox potentials of the mononuclear transition metal complexes of iron, nickel and manganese in proteins and/or their model compounds. This is particularly useful for TMCs where experimental values of the redox potentials are unavailable or difficult to determine. Moreover, the B4(XQ3)LYP-approach would be very useful for organometallic chemists, which could thereby obtain the redox potential values and ground state multiplicities of interesting TMCs before they are synthesized.

Currently the B4(XQ3)LYP-approach is intended to be applied for the calculation of the redox potentials of the heme model systems. An appropriate preliminary computational study on the structure and energetics of such a system is already done by author[121] so that the know-how can be furthermore used.

In the near future an extension of the B4(XQ3)LYP-approach to the multinuclear TMCs is planned. Preliminary results (unpublished) show, that the B4(XQ3)LYP-approach in its present form is working also for these systems, in case the involved transition metal atoms are not anti-ferromagnetically coupled with each other. However, in most of the cases multinuclear TMCs exhibit the anti-ferromagnetic coupling, in which the spin vectors associated with individual metal atoms are in opposite orientations. DFT, being a single-determinant method, does not account for the contribution of the spin-coupling between the transition metal centers. In practice, however, the broken-symmetry approach developed by Noodleman[155] helps to overcome this deficiency of DFT. In this context the B4(XQ3)LYP-approach will be configured and optimized to account for spin-coupling contributions, based on the broken-symmetry approach. Undoubtedly, such an extension would expand the application range of the B4(XQ3)LYP-approach. Particularly, the redox- and spin-properties of the Ni-Fe and poly-Mn complexes associated with important systems such as the Ni-Fe hydrogenases and photosystem II, respectively, could be computed.